

Optically Readable Organic Electrochemical Synaptic Transistors for Neuromorphic Photonic Image Processing

Yunchao Xu, Yiming Shi, Chuan Qian, Pengshan Xie, Chenxing Jin, Xiaofang Shi, Gengming Zhang, Wanrong Liu, Changjin Wan, Johnny C. Ho, Jia Sun,* and Junliang Yang*



Cite This: *Nano Lett.* 2023, 23, 5264–5271



Read Online

ACCESS |

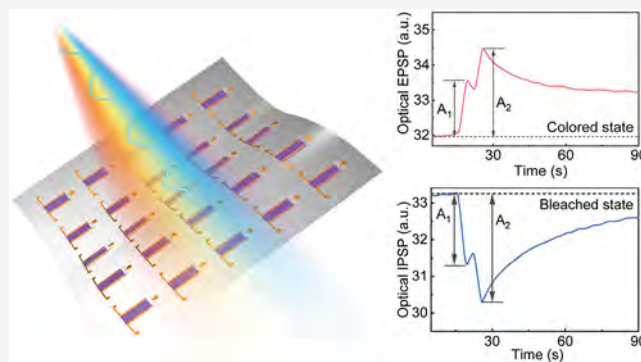
Metrics & More

Article Recommendations

Supporting Information

ABSTRACT: Optically readable organic synaptic devices have great potential in both artificial intelligence and photonic neuromorphic computing. Herein, a novel optically readable organic electrochemical synaptic transistor (OR-OEST) strategy is first proposed. The electrochemical doping mechanism of the device was systematically investigated, and the basic biological synaptic behaviors that can be read by optical means are successfully achieved. Furthermore, the flexible OR-OESTs are capable of electrically switching the transparency of semiconductor channel materials in a nonvolatile manner, and thus the multilevel memory can be achieved through optical readout. Finally, the OR-OESTs are developed for the preprocessing of photonic images, such as contrast enhancement and denoising, and feeding the processed images into an artificial neural network, achieving a recognition rate of over 90%. Overall, this work provides a new strategy for the implementation of photonic neuromorphic systems.

KEYWORDS: organic electrochemical transistors, electrochemical doping, optically readable synapses, artificial neuromorphic systems



Traditional computers based on the von Neumann architecture are less efficient in parallel computing and adaptive learning and cannot meet the urgent demand for efficient, high-speed computing.^{1,2} Brain-inspired neuromorphic computing has the advantages of high efficiency and ultralow power consumption due to its high parallelism and human brain like processing capability, which are considered as an ideal way to break the limitations of traditional computers and realize a new generation of artificial intelligence.^{3–7} Thus, neuromorphic devices are the hardware building blocks for implementing neuromorphic computing and the key to build neuromorphic chips.

In recent years, various semiconducting materials have been used to build synaptic devices for neuromorphic computing, including metal oxides,^{8–10} perovskites,^{11–15} and low-dimensional materials.^{16–19} Additionally, organic semiconducting materials are ideal materials for preparing large-area flexible integrated optoelectronic transistors, which can combine the advantages of their inherent flexibility, lightness, ease of processability, and the ability to tune the performance through molecular design.^{20–22} Among them, organic electrochemical synaptic transistors offer the advantages of a low voltage, a continuously adjustable memory, and a high compatibility for biological applications.^{23–28} Previous reports have mostly focused on electrically stimulated and light-stimulated organic synaptic devices. However, the signal readout among most of

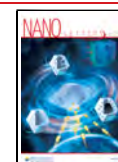
these devices is still electrically operated.^{24,29–33} Optical signals as the transmission carrier of synapses are more suitable for ultrahigh computational speed because they have unique advantages including high bandwidth, low power computation, and low crosstalk.^{34,35} More importantly, optically readable organic synapses with temporary memory can process images in real time, which can reduce the time latency of photonic neuromorphic systems. However, organic synaptic devices with optically readable capability remain unexplored.^{36–38}

Herein, we first report a new type of optically readable organic electrochemical synaptic transistor (OR-OESTs) in which an ion-gel electrolyte and poly(3-hexylthiophene-2,5-diyl) (P3HT) are used as the gate dielectric layer and the channel layer, respectively, and the coloring states of the channel layer at different wavelengths are controlled by the gate voltage (V_{gs}). The functions of basic synaptic behaviors that enable optical readout have been perfectly mimicked, such as excitatory/inhibitory postsynaptic potential (EPSP/IPSP), short-term/long-term memory (STM/LTM), and paired-pulse

Received: April 6, 2023

Revised: May 22, 2023

Published: May 25, 2023



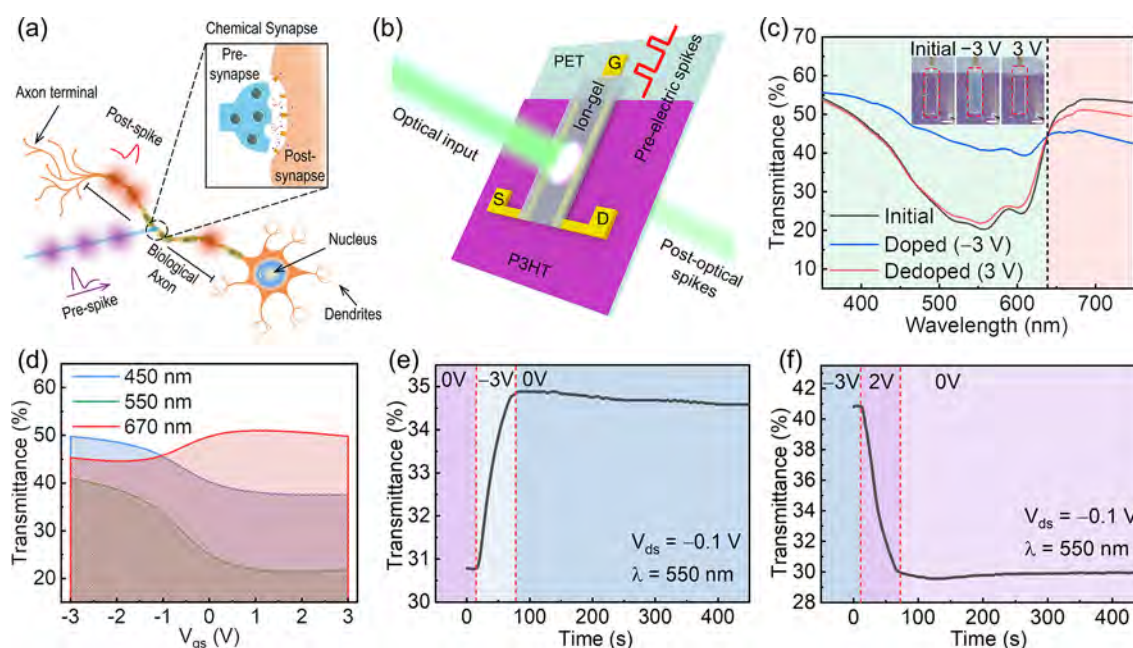


Figure 1. (a) Schematic of a biological synapse, where the communication between synapses occurs through the axonal propagation of action potentials and the release of neurotransmitters. (b) Schematic of the proposed ion-gel-gated P3HT-channel OR-OESTs. (c) Transmittance spectra of the P3HT films under electrical bias. Inset: optical microscopy images of an OR-OEST (the scale bar represents 2 mm). (d) Transmittance spectra of the P3HT films as a function of V_{gs} for different light wavelengths. (e, f) Optical transmittance of device excited by different V_{gs} .

facilitation/depression (PPF/PPD). Furthermore, the proposed OR-OEST array enables preprocessing of the photonic image, such as contrast enhancement and denoising. Consequently, the reported strategy provides a brand-new perspective for next-generation photonic neuromorphic systems.

As illustrated in Figure 1a, the synapse is the site at which neurons are functionally linked as well as an important unit for conveying information.^{39–41} The structure of OR-OESTs on a flexible polyethylene terephthalate (PET) substrate is shown in Figure 1b. The chemical structure of P3HT and the ion-gel electrolyte are illustrated in Figure S1. The self-assembled freestanding P3HT films are transferred to the PET substrates, and then, the ion-gel films are screen-printed onto the in-plane gate to complete the fabrication of the OR-OESTs, as shown in Figure S2 (detailed information is provided in the Experimental Section in the Supporting Information). The color of the P3HT film changes when different V_{gs} amplitudes are applied to the device. In the colored state of the OR-OESTs, the P3HT films have a high light absorbance, leading to a decrease in the light output intensity. In contrast, the light output intensity increases in the bleached state of the OR-OESTs. Hence, the electrical pulses are similar to the presynaptic potential spikes that occur in biological synapses. The light output and its anterior–posterior intensity variation directly correspond to the postsynaptic spikes and the synaptic weight change, respectively. Therefore, the induced changes in the optical properties of the OR-OESTs under application of the V_{gs} can be used to mimic various biological synaptic behaviors. The representative transmittance spectra of the P3HT in the visible (Vis) range at different applied V_{gs} amplitudes are depicted in Figure 1c, and the test system is schematically displayed in Figure S3. It should be noted that as the V_{gs} changes from 0 V (initial state) to -3 V, the transmittance in the 350–638 nm band increases while that in the 638–750 nm band decreases. Upon reversing the polarity

of the applied V_{gs} (i.e., 3 V), the transmittance spectra almost fully resume their original shapes. The inset of Figure 1c shows that the initial color of the P3HT film is purple; the film is bleached upon application of a negative V_{gs} (-3 V), and it resumes the purple color upon application of a positive V_{gs} (3 V). Figure 1d depicts the Vis transmittance spectra as a function of V_{gs} . The transmittance was measured at different light wavelengths (namely 450, 550, and 670 nm) as the applied V_{gs} was swept from -3 to 3 V with the drain voltage (V_{ds}) fixed at -0.1 V. It can be seen that with the increase in V_{gs} , the transmittance of 450 and 550 nm light decreases gradually while that of 670 nm light increases gradually. Furthermore, as observed in Figure 1e,f, the transmittance of the P3HT films at a light wavelength of 550 nm is not restored immediately when V_{gs} is removed (i.e., the OFF state). Therefore, the device exhibits some retention ability, indicating a memory effect by optical means.

To explore the electrochemical doping mechanism of the proposed synaptic device, further characterization of the optical, compositional, and structural changes of the film at different V_{gs} amplitudes is required. Figure 2a shows the Raman spectrum of the initial P3HT film. The strong Raman band at 1445 cm^{-1} and the weak band at 1380 cm^{-1} demonstrate the presence of neutral P3HT in the device. The peak at 1445 cm^{-1} is attributed to the $C_{\alpha}=C_{\beta}$ stretching vibration, whereas the band at 1386 cm^{-1} is attributed to the $C_{\beta}-C_{\beta}$ stretching vibration of the aromatic thiophene ring.^{42,43} At $V_{gs} = -1$ V, the two peaks shift to 1438 and 1379 cm^{-1} , respectively. At $V_{gs} = -3$ V, the two peaks shift even further to 1406 and 1373 cm^{-1} , respectively. The Raman images associated with the different V_{gs} amplitudes indicate that the electrochemical doping-induced charge in the polymer semiconductor leads to the formation of polarons and/or bipolarons.⁴⁴ The schematic chemical structure of P3HT in the neutral and doped states is shown in Figure S4. Upon doping, with the formation of positive charges on the polymer

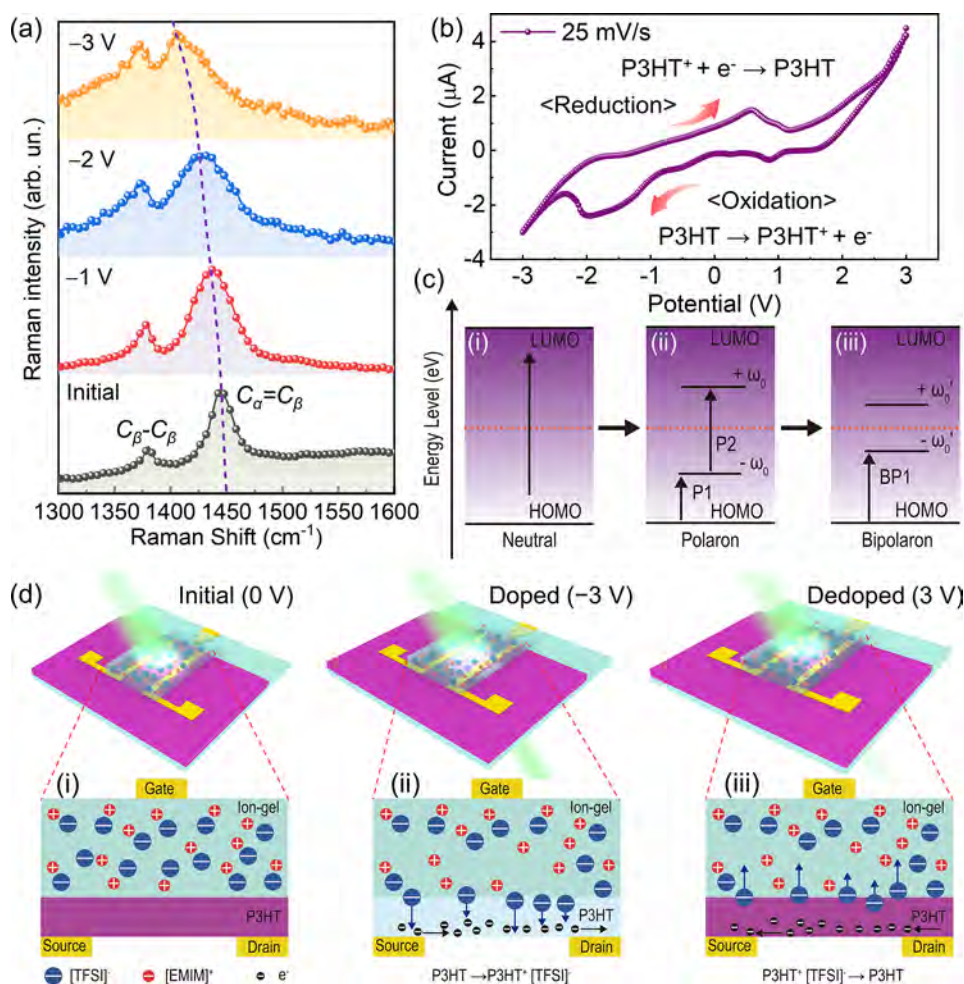


Figure 2. (a) In situ Raman spectra of the P3HT film in its initial state and under -1 , -2 , and -3 V. (b) Cyclic voltammogram of the ion-gel-gated P3HT-channel organic electrochemical transistor. (c) Schematic energy level diagram of the device at different doping levels. (d) Schematic of the modulation mechanism of the device under different V_{gs} amplitudes.

chains, the chemical structure of the neutral P3HT changes from benzoid-like to quinoid-like. Figure 2b displays the cyclic voltammogram ($C-V$) of the OR-OESTs in the potential range between 3 and -3 V. In this $C-V$ curve, the peak at -1.97 V (oxidation peak) indicates the oxidation of P3HT to the polaron and bipolaron states while the peak at 0.6 V (reduction peak) indicates the change from the polaron and bipolaron states to the neutral state. Furthermore, absorption spectroscopic measurements were conducted to quantify the color differences under different V_{gs} amplitudes (Figure S5). The observed absorption spectral changes of P3HT under different V_{gs} amplitudes can be explained by the energy level diagram (Figure 2c). The electron transition from the highest occupied molecular orbital (HOMO) to the lowest unoccupied molecular orbital (LUMO) corresponds to the absorption band of P3HT at $400-630$ nm (Figure 2c(i)). As shown in Figure 2c(ii), when the polarons are formed, two localized electronic states are created ($+\omega_0$ and $-\omega_0$), and the absorption band of P3HT in the ultraviolet (UV)/Vis range can be assigned to the polaron state transition P_2 from the $-\omega_0$ level to the $+\omega_0$ level, while the near-infrared (NIR) absorption band can be assigned to the polar state transition P_1 . The polaron is formed at the initial stage of doping; however, at a later stage of doping, a bipolaron is formed ($+\omega'_0$ and $-\omega'_0$ levels). Thus, the NIR absorption band of P3HT can be

assigned to the polaron state transition BP_1 ; at the maximum doping level, only the bipolaron is present (Figure 2c(iii)).^{45,46} In order to verify the correctness of the doping mechanism, we demonstrated the presence of ion doping via scanning electron microscopy (SEM), SEM-energy dispersive X-ray spectroscopy (SEM-EDS), and X-ray photoelectron spectroscopy (XPS), as shown in Figures S6 and S7. These results provide strong evidence of the occurrence of an electrochemical reaction due to the penetration of negative ions ($[TFSI]^-$) into the P3HT layer. Figure 2d shows a schematic of the formation mechanism of the colored/bleached states in our device. During the resting stage, anions and cations are randomly distributed in the ion-gel electrolyte (Figure 2d(i)). When a negative V_{gs} (-3 V) is applied to the gate electrode, electrons are extracted from P3HT and flow to the drain electrode while the $[TFSI]^-$ ions are pumped from the ion-gel electrolyte to the P3HT layer to maintain charge neutrality. This creates $n[P3HT]^+m[TFSI]^-$ and eventually leads to the oxidation of the P3HT film (Figure 2d(ii)). In this process, the film becomes pale blue (bleached state), and the optical transmittance at $400-638$ nm increases considerably. Conversely, when a positive V_{gs} (3 V) is applied to the gate electrode, electrons are injected while $[TFSI]^-$ ions are extracted from the $n[P3HT]^+m[TFSI]^-$ host (Figure 2d(iii)). This reduces the $n[P3HT]^+m[TFSI]^-$ content and restores the original state

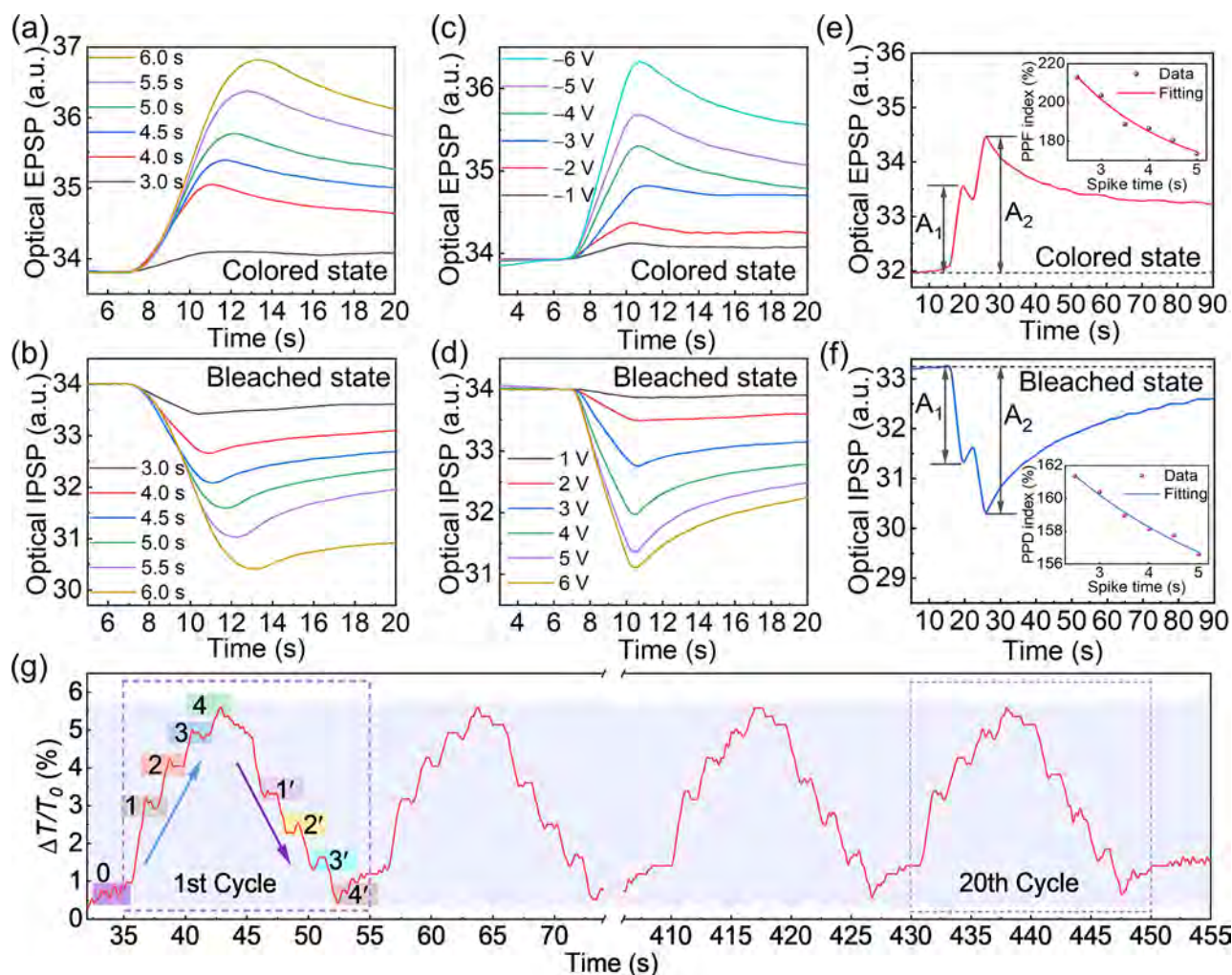
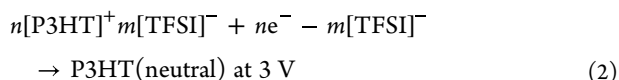
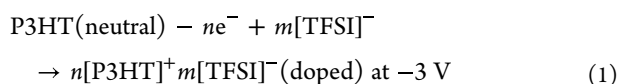


Figure 3. (a) Optical EPSP responses as a function of the electrical pulse width (fixed $V_{gs} = -3$ V, $V_{ds} = -0.1$ V). (b) Optical IPSP responses as a function of the electrical pulse width (fixed $V_{gs} = 3$ V, $V_{ds} = -0.1$ V). (c) Optical EPSP responses triggered by electrical pulses of different amplitudes, ranging from -1 to -6 V (fixed pulse width of 4 s, $V_{ds} = -0.1$ V). (d) Optical IPSP responses triggered by electrical pulses of different amplitudes, ranging from 1 to 6 V (fixed pulse width of 4 s, $V_{ds} = -0.1$ V). (e) Optical EPSP and (f) IPSP responses triggered by a pair of electrical pulses separated by $\Delta t = 5$ s (fixed pulse width of 1 s, $V_{gs} = -3$ V for EPSP, and 3 V for IPSP, $V_{ds} = -0.1$ V). Inset: PPF index and PPD index as a function of Δt . (g) Percentage change in the electromodulated transmittance during continuous switching cycles between the colored/bleached states.

of the P3HT film, which recovers its purple color (colored state), and the optical transmittance is restored. The redox reactions in the device can be expressed as follows:



As shown in eqs 1 and 2, due to electrochemical oxidation or reduction, the change in the electronic structure of P3HT alters its optical absorption, leading to a change in the color of the P3HT film.

As far as the OR-OESTs are concerned, the external stimulation refers to the V_{gs} and the action potential in biological synapses corresponds to the light output intensity. In the bleached/colored state of the device (with a high/low initial transmittance), when a negative/positive V_{gs} pulse is applied, the optical postsynaptic potential increases/decreases

due to ion doping/dedoping, which reduces/enhances the loss of light absorption. Therefore, this potential can be defined as an optical EPSP/IPSP. As displayed in Figure 3a,b, for a given input light intensity, the different output light intensities caused by the different durations of the electrical pulses represent different synaptic weights, which indicate the transition from the STM to the LTM. Likewise, as can be seen from Figure 3c,d, the memory retention time of the proposed device is significantly prolonged as the amplitude of the electrical pulses increases. These results suggest that the OR-OESTs can successfully implement the synaptic plasticity and memory behavior of the human brain. In addition, there is similar optical synaptic plasticity at other wavelengths (450 and 670 nm), as shown in Figure S8. As illustrated in Figure 3e,f, the pair of presynaptic spikes (V_{gs}) varied with the optical EPSP and IPSP amplitudes in the colored and bleached states, respectively. The relationship between the optical EPSP/IPSP amplitudes and two consecutive V_{gs} pulses separated by an interval time (Δt) was also investigated, as shown in Figure S9.

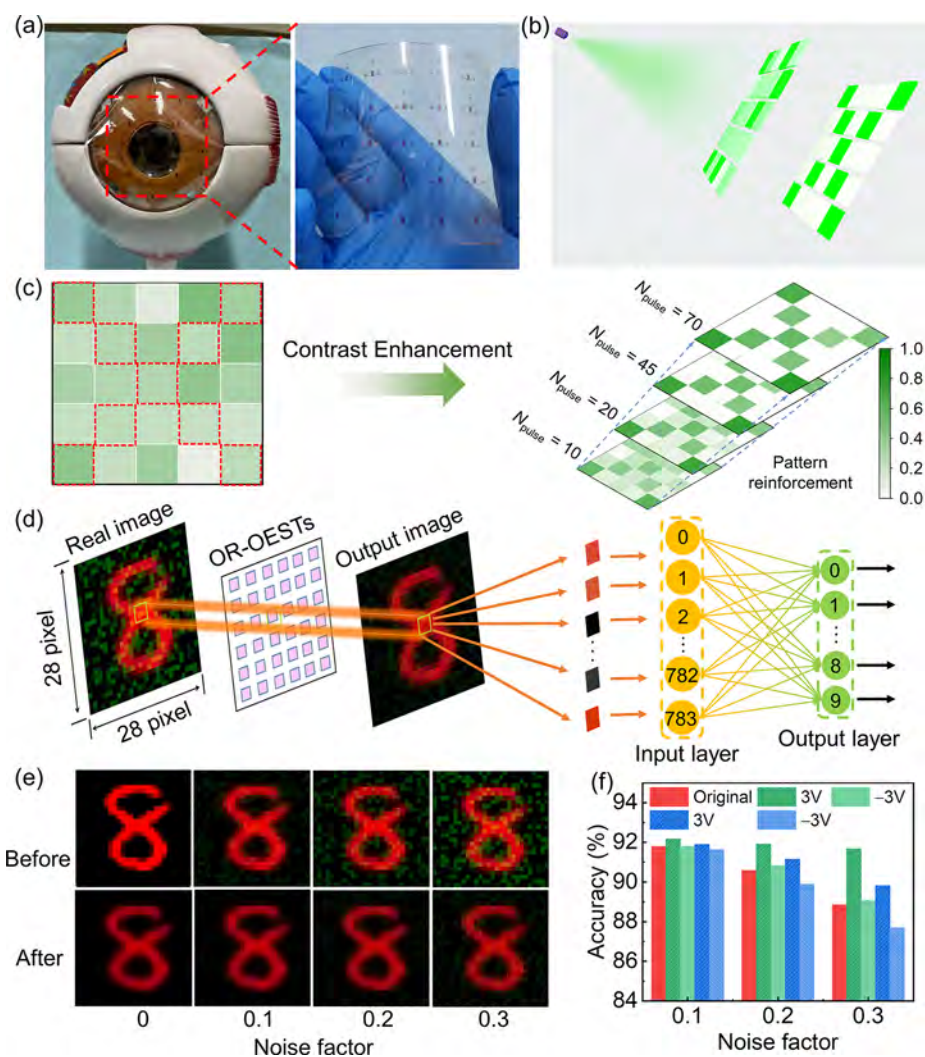


Figure 4. (a) Photos of the flexible OR-OEST array attached to the human eyeball model. (b) Contrast enhancement achieved with a 5×5 OR-OEST array. (c) Results of output maps in the initial state and after pulse numbers of 10, 20, 45, and 70, respectively. (d) Schematics of the OR-OEST devices for photonic image denoising and an artificial neural network for photonic image recognition. (e) MNIST images with different noise factors before and after OR-OEST array preprocessing. (f) Comparison of the MNIST image recognition rate with and without OR-OEST array preprocessing at different V_{gs} amplitudes.

The PPF and PPD indexes are defined according to the equation

$$\text{PPF or PPD} = \frac{A_2}{A_1} \times 100\% \quad (3)$$

where A_1 and A_2 are the absolute values of the first and second spikes of the optical postsynaptic potential, respectively. The insets in Figure 3e,f display the relationship between the PPF/PPD index and Δt in the colored and bleached states of the device, respectively. Clearly, the PPF or PPD index decays rapidly with increasing Δt , and the data can be fitted according to the equation

$$\text{PPF/PPD index} = C_1 \exp(-\Delta t/\tau_1) + C_0 \quad (4)$$

where C_0 is a constant, C_1 is the initial facilitation magnitude, and τ_1 is the characteristic relaxation time. According to the fitting results, $C_1 = 180\%$ (18.7%) and $\tau_1 = 2.15$ s (3.87 s) in the colored (bleached) state of the OR-OESTs. This result indicates that the optical intensity of the OR-OESTs has a strong temporal dependence, which is largely consistent with the behavior of biological synapses.

To evaluate the behavior of the multilevel optical memory and cyclic stability of this device, the temporal behavior of the optical memory level was investigated (Figure 3g). The optical transmittance (T_0) of the device is defined as the baseline of the readout and assigned to an optical synaptic weight “0” (colored state). Any subsequent change of the readout ($\Delta T = T - T_0$) during the measurement is normalized as the relative change in percentage ($\Delta T/T_0$) to the baseline. The device started at weight “0”, which then reaches weights of “1”, “2”, “3”, and “4”, upon application of four V_{gs} pulses (amplitude -3 V, pulse duration 1 s, $\Delta t = 1$ s), respectively. A multilevel photonic memory state is thus obtained starting from the colored state of the OR-OESTs to the bleached state. Similarly, when the device starts at weight “4” (bleached state), it reaches weights “1”, “2”, “3”, and “4”, upon application of four V_{gs} pulses with amplitude 2 V, pulse duration 1 s, and $\Delta t = 1$ s, respectively. After 20 cycles, the devices still exhibit high cyclic stability (Figure S10). The optical long-term potentiation (LTP) and long-term depression (LTD) of the proposed device were investigated (Figure S11). These results imply that

the optical memory level can be tuned by varying the number of V_{gs} pulses.

To investigate the image preprocessing capabilities of the OR-OESTs, a 5×5 device array was fabricated. An image of an array attached to the human eyeball model and photos of the flexible OR-OESTs are illustrated in Figure 4a. Furthermore, we evaluated the electrical characteristics of all 25 devices in the flexible OR-OESTs, and 100% of the devices exhibited typical transistor characteristics with a large current on/off ratio of $>10^4$ and hysteresis window of >1.2 V (Figures S12 and S13). The electrical performance under bending conditions is only slightly changed, which indicates that the OR-OESTs have excellent stability and reliability (Figures S14). In an image classification task, image preprocessing is critical for optimizing features from a large amount of original data and reducing redundancy.⁴⁷ All light intensities were normalized (Figure S11), and a 550 nm green light was randomly illuminated onto the whole array with an intensity ranging from 0 to 0.5, as shown in Figure 4b. We divided the OR-OEST array into two regions: image of optical pattern “X” and the remaining (Figure 4c). The former with V_{gs} amplitudes of -3 V pulse and the latter with amplitudes 2 V pulse, respectively, are continuously input into the array. As the number of pulses increases, the transmittance increases with the negative V_{gs} (-3 V) pulses imposed, while it decreases with the application of positive V_{gs} (2 V) pulses (Figure S11). Figure 4c shows output maps after 10, 20, 45, and 70 pulses. It was found that the output pattern “X” became more distinct as the number of pulses increased. This means the OR-OEST array can highlight the differences and extract information more efficiently. In addition to contrast enhancement, denoising plays an important role in image classification. In this preprocessing step, the red (R)–green (G)–blue (B) values were mapped to the intensities of light pulses with wavelengths of 670, 550, and 450 nm, respectively. To illustrate the denoising capability of the OR-OESTs array, we propose an artificial photonic neuromorphic system (784 inputs and 10 outputs), as shown in Figure 4d. To demonstrate the difference in photonic image classification with and without the OR-OESTs array, we used the standard 28×28 pixel Modified National Institute of Standards and Technology (MNIST) data set with noise. The photonic image passes through the OR-OEST array (one image pixel corresponds to one device). In previous works on image preprocessing, devices have been usually only designed to extract a particular wavelength feature in a specific situation.^{48–51} To prove that the proposed OR-OEST array can perform well in a variety of situations, we combined 450, 550, and 670 nm wavelengths of light in pairs, with one wavelength as the optical pattern “8” and the other wavelength as the background noise, and V_{gs} values ranging from 3 to -3 V were applied to the OR-OEST array. The optical pattern “8” is red with a green background noise generated according to a Gaussian distribution. For a given $V_{gs} = 3$ V, the OR-OEST array exhibits different transmittances for red, green, and blue light, with the red light transmittance being the highest. When a positive V_{gs} (3 V) is applied to the OR-OEST array, the red pixels pass through while the green background noise is filtered out. The input and output images after denoising are compared in Figure 4e, where the noise factor varies from 0 to 0.3. The denoising results of the red optical pattern “8” by changing the V_{gs} or background noise are displayed in Figures S15 and S16. After denoising, we fed the processed data sets into an artificial

neural network. We tested the recognition rate of the red optical pattern “8” with different wavelengths of background noises at different V_{gs} amplitudes. Figure 4f illustrates the recognition rate after image preprocessing. The figure shows that the photonic image preprocessing with the OR-OEST array at high noise coefficients results in a significant increase in the recognition rate. When the noise factor is 0.3, the recognition rate after 100 epochs is 88.86% without the OR-OEST array preprocessing, and it can be improved to 91.68% after preprocessing. We changed the color of the optical pattern “8” and the background noise for denoising and recognition. The recognition rate of the green (blue) optical pattern “8” with either blue or red (green or red) background noise at different V_{gs} amplitudes is shown in Figure S17 (Figure S18). Overall, the recognition rate of red and blue optical images was significantly improved after denoising. These results demonstrate the superiority of the OR-OESTs over conventional optoelectronic synaptic transistors for photonic image preprocessing.

In this study, we proposed a flexible OR-OEST for the first time. The electrically driven movement of $[TFSI]^-$ ions in the electrolyte changes the interaction strength between light and the P3HT film, thus permitting the optical tuning of the synaptic connection strength. The proposed OR-OESTs mimic the basic biological synaptic behaviors using optical means. Furthermore, we utilized arrays of the proposed OR-OESTs to realize photonic image preprocessing, in particular, contrast enhancement and denoising. Therefore, our devices would provide a promising concept for an organic photonic neuromorphic system.

■ ASSOCIATED CONTENT

Supporting Information

The Supporting Information is available free of charge at <https://pubs.acs.org/doi/10.1021/acs.nanolett.3c01291>.

Experimental details, UV–vis absorption spectra, XPS, and SEM of P3HT films, experimental data for synaptic functionality, and additional figures for photonic image preprocessing (PDF)

■ AUTHOR INFORMATION

Corresponding Authors

Jia Sun – Hunan Key Laboratory for Super Microstructure and Ultrafast Process, School of Physics and Electronics, Central South University, Changsha, Hunan 410083, People’s Republic of China; Hunan Key Laboratory of Nanophotonics and Devices, School of Physics and Electronics, Central South University, Changsha, Hunan 410083, People’s Republic of China; orcid.org/0000-0003-4423-8128; Email: jiasun@csu.edu.cn

Junliang Yang – Hunan Key Laboratory for Super Microstructure and Ultrafast Process, School of Physics and Electronics, Central South University, Changsha, Hunan 410083, People’s Republic of China; Hunan Key Laboratory of Nanophotonics and Devices, School of Physics and Electronics, Central South University, Changsha, Hunan 410083, People’s Republic of China; orcid.org/0000-0002-5553-0186; Email: junliang.yang@csu.edu.cn

Authors

Yunchao Xu – Hunan Key Laboratory for Super Microstructure and Ultrafast Process, School of Physics and

Electronics, Central South University, Changsha, Hunan 410083, People's Republic of China; Hunan Key Laboratory of Nanophotonics and Devices, School of Physics and Electronics, Central South University, Changsha, Hunan 410083, People's Republic of China

Yiming Shi – Hunan Key Laboratory for Super Microstructure and Ultrafast Process, School of Physics and Electronics, Central South University, Changsha, Hunan 410083, People's Republic of China; Hunan Key Laboratory of Nanophotonics and Devices, School of Physics and Electronics, Central South University, Changsha, Hunan 410083, People's Republic of China

Chuan Qian – Low-dimensional Quantum Structures and Quantum Control of Ministry of Education, Department of Physics, Hunan Normal University, Changsha, Hunan 410081, People's Republic of China

Pengshan Xie – Department of Materials Science and Engineering, City University of Hong Kong, Kowloon, Hong Kong SAR 999077, People's Republic of China


Chenxing Jin – Hunan Key Laboratory for Super Microstructure and Ultrafast Process, School of Physics and Electronics, Central South University, Changsha, Hunan 410083, People's Republic of China; Hunan Key Laboratory of Nanophotonics and Devices, School of Physics and Electronics, Central South University, Changsha, Hunan 410083, People's Republic of China

Xiaofang Shi – Hunan Key Laboratory for Super Microstructure and Ultrafast Process, School of Physics and Electronics, Central South University, Changsha, Hunan 410083, People's Republic of China; Hunan Key Laboratory of Nanophotonics and Devices, School of Physics and Electronics, Central South University, Changsha, Hunan 410083, People's Republic of China

Gengming Zhang – Hunan Key Laboratory for Super Microstructure and Ultrafast Process, School of Physics and Electronics, Central South University, Changsha, Hunan 410083, People's Republic of China

Wanrong Liu – Hunan Key Laboratory for Super Microstructure and Ultrafast Process, School of Physics and Electronics, Central South University, Changsha, Hunan 410083, People's Republic of China; Hunan Key Laboratory of Nanophotonics and Devices, School of Physics and Electronics, Central South University, Changsha, Hunan 410083, People's Republic of China

Changjin Wan – School of Electronic Science & Engineering, and Collaborative Innovation Centre of Advanced Microstructures, Nanjing University, Nanjing, Jiangsu 210008, People's Republic of China

Johnny C. Ho – Department of Materials Science and Engineering, City University of Hong Kong, Kowloon, Hong Kong SAR 999077, People's Republic of China;
 orcid.org/0000-0003-3000-8794

Complete contact information is available at:
<https://pubs.acs.org/10.1021/acs.nanolett.3c01291>

Author Contributions

Y.X. and Y.S. contributed equally.

Notes

The authors declare no competing financial interest.

ACKNOWLEDGMENTS

This study has been supported by the National Natural Science Foundation of China (Nos. 61975241 and 52173192), the Huxiang Youth Talent Program of Hunan Province (No. 2020RC3010), the Science and Technology Innovation Program of Hunan Province (No. 2021RC2077), the National Key Research and Development Program of China (No. 2022YFB3803300), and the Fundamental Research Funds for the Central Universities of Central South University (No. 1053320213517).

REFERENCES

- (1) Von Neumann, J. First Draft of a Report on the EDVAC. *IEEE Ann. Hist. Comput.* **1993**, *15* (4), 27–75.
- (2) Zidan, M. A.; Strachan, J. P.; Lu, W. D. The future of electronics based on memristive systems. *Nat. Electron.* **2018**, *1* (1), 22–29.
- (3) Van De Burgt, Y.; Lubberman, E.; Fuller, E. J.; Keene, S. T.; Faria, G. C.; Agarwal, S.; Marinella, M. J.; Alec Talin, A.; Salleo, A. A non-volatile organic electrochemical device as a low-voltage artificial synapse for neuromorphic computing. *Nat. Mater.* **2017**, *16* (4), 414–418.
- (4) Zhu, C.; Liu, H.; Wang, W.; Xiang, L.; Jiang, J.; Shuai, Q.; Yang, X.; Zhang, T.; Zheng, B.; Wang, H.; et al. Optical synaptic devices with ultra-low power consumption for neuromorphic computing. *Light: Sci. Appl.* **2022**, *11* (1), 337.
- (5) Liu, G. C.; Li, Q. Y.; Shi, W.; Liu, Y. W.; Liu, K.; Yang, X. L.; Shao, M. C.; Guo, A. K.; Huang, X.; Zhang, F.; et al. Ultralow-Power and Multisensory Artificial Synapse Based on Electrolyte-Gated Vertical Organic Transistors. *Adv. Funct. Mater.* **2022**, *32* (27), 2200959.
- (6) Choi, Y.; Oh, S.; Qian, C.; Park, J. H.; Cho, J. H. Vertical organic synapse expandable to 3D crossbar array. *Nat. Commun.* **2020**, *11* (1), 4595.
- (7) Li, Q.; Wang, T.; Fang, Y.; Hu, X.; Tang, C.; Wu, X.; Zhu, H.; Ji, L.; Sun, Q. Q.; Zhang, D. W.; et al. Ultralow Power Wearable Organic Ferroelectric Device for Optoelectronic Neuromorphic Computing. *Nano Lett.* **2022**, *22* (15), 6435–6443.
- (8) Feng, G.; Jiang, J.; Zhao, Y.; Wang, S.; Liu, B.; Yin, K.; Niu, D.; Li, X.; Chen, Y.; Duan, H.; et al. A sub-10 nm vertical organic/inorganic hybrid transistor for pain-perceptual and sensitization-regulated nociceptor emulation. *Adv. Mater.* **2020**, *32* (6), 1906171.
- (9) Kim, S.; Jo, S. B.; Kim, J.; Rhee, D.; Choi, Y. Y.; Kim, D. H.; Kang, J.; Cho, J. H. Gate-Deterministic Remote Doping Enables Highly Retentive Graphene-MXene Hybrid Memory Devices on Plastic. *Adv. Funct. Mater.* **2022**, *32* (20), 2111956.
- (10) Chen, C.; He, Y.; Mao, H.; Zhu, L.; Wang, X.; Zhu, Y.; Zhu, Y.; Shi, Y.; Wan, C.; Wan, Q. A Photoelectric Spiking Neuron for Visual Depth Perception. *Adv. Mater.* **2022**, *34* (20), No. 2201895.
- (11) Jeong, B.; Gkoupidenis, P.; Asadi, K. Solution-Processed Perovskite Field-Effect Transistor Artificial Synapses. *Adv. Mater.* **2021**, *33* (52), No. 2104034.
- (12) Xu, W.; Cho, H.; Kim, Y. H.; Kim, Y. T.; Wolf, C.; Park, C. G.; Lee, T. W. Organometal Halide Perovskite Artificial Synapses. *Adv. Mater.* **2016**, *28* (28), 5916–5922.
- (13) Yang, B.; Lu, Y.; Jiang, D.; Li, Z.; Zeng, Y.; Zhang, S.; Ye, Y.; Liu, Z.; Ou, Q.; Wang, Y.; et al. Bioinspired Multifunctional Organic Transistors Based on Natural Chlorophyll/Organic Semiconductors. *Adv. Mater.* **2020**, *32* (28), No. 2001227.
- (14) Xing, J.; Zhao, C.; Zou, Y.; Kong, W.; Yu, Z.; Shan, Y.; Dong, Q.; Zhou, D.; Yu, W.; Guo, C. Modulating the optical and electrical properties of MAPbBr₃ single crystals via voltage regulation engineering and application in memristors. *Light: Sci. Appl.* **2020**, *9* (1), 111.
- (15) Wang, Y.; Lv, Z.; Chen, J.; Wang, Z.; Zhou, Y.; Zhou, L.; Chen, X.; Han, S. T. Photonic Synapses Based on Inorganic Perovskite Quantum Dots for Neuromorphic Computing. *Adv. Mater.* **2018**, *30* (38), No. 1802883.

- (16) Sangwan, V. K.; Lee, H. S.; Bergeron, H.; Balla, I.; Beck, M. E.; Chen, K. S.; Hersam, M. C. Multi-terminal memtransistors from polycrystalline monolayer molybdenum disulfide. *Nature* **2018**, *554* (7693), 500–504.
- (17) Sun, J.; Choi, Y.; Choi, Y. J.; Kim, S.; Park, J. H.; Lee, S.; Cho, J. H. 2D-organic hybrid heterostructures for optoelectronic applications. *Adv. Mater.* **2019**, *31* (34), 1803831.
- (18) Yu, J. R.; Yang, X. X.; Gao, G. Y.; Xiong, Y.; Wang, Y. F.; Han, J.; Chen, Y. H.; Zhang, H.; Sun, Q. J.; Wang, Z. L. Bioinspired mechano-photonics artificial synapse based on graphene/MoS₂ heterostructure. *Sci. Adv.* **2021**, *7* (12), No. eabd9117.
- (19) Wang, B.; Wang, X.; Wang, E.; Li, C.; Peng, R.; Wu, Y.; Xin, Z.; Sun, Y.; Guo, J.; Fan, S.; et al. Monolayer MoS₂ Synaptic Transistors for High-Temperature Neuromorphic Applications. *Nano Lett.* **2021**, *21* (24), 10400–10408.
- (20) Rivnay, J.; Inal, S.; Salleo, A.; Owens, R. M.; Berggren, M.; Malliaras, G. G. Organic electrochemical transistors. *Nat. Rev. Mater.* **2018**, *3* (2), 1–14.
- (21) Wang, Y.; Sun, L.; Wang, C.; Yang, F.; Ren, X.; Zhang, X.; Dong, H.; Hu, W. Organic crystalline materials in flexible electronics. *Chem. Soc. Rev.* **2019**, *48* (6), 1492–1530.
- (22) Huang, W.; Chen, J.; Yao, Y.; Zheng, D.; Ji, X.; Feng, L. W.; Moore, D.; Glavin, N. R.; Xie, M.; Chen, Y.; et al. Vertical organic electrochemical transistors for complementary circuits. *Nature* **2023**, *613* (7944), 496–502.
- (23) Ji, X.; Paulsen, B. D.; Chik, G. K. K.; Wu, R.; Yin, Y.; Chan, P. K. L.; Rivnay, J. Mimicking associative learning using an ion-trapping non-volatile synaptic organic electrochemical transistor. *Nat. Commun.* **2021**, *12* (1), 2480.
- (24) Harikesh, P. C.; Yang, C. Y.; Tu, D.; Gerasimov, J. Y.; Dar, A. M.; Armada-Moreira, A.; Massetti, M.; Kroon, R.; Bliman, D.; Olsson, R.; et al. Organic electrochemical neurons and synapses with ion mediated spiking. *Nat. Commun.* **2022**, *13* (1), 901.
- (25) Zhao, Y. F.; Su, C. H.; Shen, G. Y.; Xie, Z. C.; Xiao, W.; Fu, Y. J.; Inal, S.; Wang, Q.; Wang, Y. Z.; Yue, W.; et al. Donor Engineering Tuning the Analog Switching Range and Operational Stability of Organic Synaptic Transistors for Neuromorphic Systems. *Adv. Funct. Mater.* **2022**, *32* (36), 2205744.
- (26) Kim, Y.; Chortos, A.; Xu, W.; Liu, Y.; Oh, J. Y.; Son, D.; Kang, J.; Foudeh, A. M.; Zhu, C.; Lee, Y.; et al. A bioinspired flexible organic artificial afferent nerve. *Science* **2018**, *360* (6392), 998–1003.
- (27) Shi, J. L.; Jie, J. S.; Deng, W.; Luo, G.; Fang, X. C.; Xiao, Y. L.; Zhang, Y. J.; Zhang, X. J.; Zhang, X. H. A Fully Solution-Printed Photosynaptic Transistor Array with Ultralow Energy Consumption for Artificial-Vision Neural Networks. *Adv. Mater.* **2022**, *34* (18), 2200380.
- (28) Eckel, C.; Lenz, J.; Melianas, A.; Salleo, A.; Weitz, R. T. Nanoscopic Electrolyte-Gated Vertical Organic Transistors with Low Operation Voltage and Five Orders of Magnitude Switching Range for Neuromorphic Systems. *Nano Lett.* **2022**, *22* (3), 973–978.
- (29) Xu, W.; Min, S. Y.; Hwang, H.; Lee, T. W. Organic core-sheath nanowire artificial synapses with femtojoule energy consumption. *Sci. Adv.* **2016**, *2* (6), No. e1501326.
- (30) Lee, Y.; Park, H. L.; Kim, Y.; Lee, T. W. Organic electronic synapses with low energy consumption. *Joule* **2021**, *5* (4), 794–810.
- (31) Shao, L.; Zhao, Y.; Liu, Y. Q. Organic Synaptic Transistors: The Evolutionary Path from Memory Cells to the Application of Artificial Neural Networks. *Adv. Funct. Mater.* **2021**, *31* (28), 2101951.
- (32) Qian, C.; Choi, Y.; Choi, Y. J.; Kim, S.; Choi, Y. Y.; Roe, D. G.; Kang, M. S.; Sun, J.; Cho, J. H. Oxygen-Detecting Synaptic Device for Realization of Artificial Autonomic Nervous System for Maintaining Oxygen Homeostasis. *Adv. Mater.* **2020**, *32* (34), 2002653.
- (33) Harikesh, P. C.; Yang, C.-Y.; Tu, D.; Gerasimov, J. Y.; Dar, A. M.; Armada-Moreira, A.; Massetti, M.; Kroon, R.; Bliman, D.; Olsson, R.; et al. Organic electrochemical neurons and synapses with ion mediated spiking. *Nat. Commun.* **2022**, *13* (1), 901.
- (34) Shastri, B. J.; Tait, A. N.; de Lima, T. F.; Pernice, W. H. P.; Bhaskaran, H.; Wright, C. D.; Prucnal, P. R. Photonics for artificial intelligence and neuromorphic computing. *Nat. Photonics* **2021**, *15* (2), 102–114.
- (35) Feldmann, J.; Youngblood, N.; Wright, C. D.; Bhaskaran, H.; Pernice, W. H. P. All-optical spiking neurosynaptic networks with self-learning capabilities. *Nature* **2019**, *569* (7755), 208–214.
- (36) Gholipour, B.; Bastock, P.; Craig, C.; Khan, K.; Hewak, D.; Soci, C. Amorphous Metal-Sulphide Microfibers Enable Photonic Synapses for Brain-Like Computing. *Adv. Opt. Mater.* **2015**, *3* (5), 635–641.
- (37) Wang, Y.; Yin, L.; Huang, W.; Li, Y. Y.; Huang, S. J.; Zhu, Y. Y.; Yang, D. R.; Pi, X. D. Optoelectronic Synaptic Devices for Neuromorphic Computing. *Adv. Intell. Syst.* **2021**, *3* (1), 2000099.
- (38) Kim, J. T.; Song, J.; Ah, C. S. Optically Readable Waveguide-Integrated Electrochromic Artificial Synaptic Device for Photonic Neuromorphic Systems. *ACS Appl. Electron. Mater.* **2020**, *2* (7), 2057–2063.
- (39) Pereda, A. E. Electrical synapses and their functional interactions with chemical synapses. *Nat. Rev. Neurosci.* **2014**, *15* (4), 250–263.
- (40) Faber, D. S.; Pereda, A. E. Two Forms of Electrical Transmission Between Neurons. *Front. Mol. Neurosci.* **2018**, *11*, 427.
- (41) Yu, J. R.; Wang, Y. F.; Qin, S. S.; Gao, G. Y.; Xu, C.; Wang, Z. L.; Sun, Q. J. Bioinspired interactive neuromorphic devices. *Mater. Today* **2022**, *60*, 158–182.
- (42) Louarn, G.; Trznadel, M.; Buisson, J. P.; Laska, J.; Pron, A.; Lapkowski, M.; Lefrant, S. Raman spectroscopic studies of regioregular poly(3-alkylthiophenes). *J. Phys. Chem.* **1996**, *100* (30), 12532–12539.
- (43) Yamamoto, J.; Furukawa, Y. Electronic and vibrational spectra of positive polarons and bipolarons in regioregular poly(3-hexylthiophene) doped with ferric chloride. *J. Phys. Chem. B* **2015**, *119* (13), 4788–4794.
- (44) Mansour, A. E.; Valencia, A. M.; Lungwitz, D.; Wegner, B.; Tanaka, N.; Shoji, Y.; Fukushima, T.; Opitz, A.; Cocchi, C.; Koch, N. Understanding the evolution of the Raman spectra of molecularly p-doped poly(3-hexylthiophene-2,5-diyl): signatures of polarons and bipolarons. *Phys. Chem. Chem. Phys.* **2022**, *24* (5), 3109–3118.
- (45) Koo, J.; Amoli, V.; Kim, S. Y.; Lee, C.; Kim, J.; Park, S. M.; Kim, J.; Ahn, J. M.; Jung, K. J.; Kim, D. H. Low-power, deformable, dynamic multicolor electrochromic skin. *Nano Energy* **2020**, *78*, 105199.
- (46) Enengl, C.; Enengl, S.; Pluczyk, S.; Havlicek, M.; Lapkowski, M.; Neugebauer, H.; Ehrenfreund, E. Doping-Induced Absorption Bands in P3HT: Polarons and Bipolarons. *ChemPhysChem* **2016**, *17* (23), 3836–3844.
- (47) Yao, P.; Wu, H.; Gao, B.; Eryilmaz, S. B.; Huang, X.; Zhang, W.; Zhang, Q.; Deng, N.; Shi, L.; Wong, H. P.; et al. Face classification using electronic synapses. *Nat. Commun.* **2017**, *8* (1), 15199.
- (48) Shao, H.; Li, Y.; Yang, W.; He, X.; Wang, L.; Fu, J.; Fu, M.; Ling, H.; Gkoupidenis, P.; Yan, F.; et al. Reconfigurable Optoelectronic Synaptic Transistor with Stable Zr-CsPbI₃ Nanocrystals for Visuomorphic Computing. *Adv. Mater.* **2023**, *35*, 2208497.
- (49) Yu, R.; He, L.; Gao, C.; Zhang, X.; Li, E.; Guo, T.; Li, W.; Chen, H. Programmable ferroelectric bionic vision hardware with selective attention for high-precision image classification. *Nat. Commun.* **2022**, *13* (1), 7019.
- (50) Li, G.; Xie, D.; Zhong, H.; Zhang, Z.; Fu, X.; Zhou, Q.; Li, Q.; Ni, H.; Wang, J.; Guo, E. J.; et al. Photo-induced non-volatile VO₂ phase transition for neuromorphic ultraviolet sensors. *Nat. Commun.* **2022**, *13* (1), 1729.
- (51) Wang, Y.; Zhu, Y. Y.; Li, Y. Y.; Zhang, Y. Q.; Yang, D. R.; Pi, X. D. Dual-Modal Optoelectronic Synaptic Devices with Versatile Synaptic Plasticity. *Adv. Funct. Mater.* **2022**, *32* (1), 2107973.